Materials Chemistry and Physics: Sustainability and Energy xxx (xxxx) 100060

Contents lists available at ScienceDirect

Materials Chemistry and Physics: Sustainability and Energy

journal homepage: www.elsevier.com

Journal logo

Halogen-free electrolyte engineering and multifunctional sulfur cathodes for rechargeable Mg–S and Na–S batteries

Manal Bin Zaima [a], Hassan Manaa [b], Osama Ragab [b], Ibrahim S. Yahia [c], Yanna NuLi [d], M.M. El-Desoky [e, *], Eslam Sheha [b, **]

[a] General Sciences Department, College of Applied Sciences, AlMaarefa University, Diriyah, 13713, Riyadh, Saudi Arabia
[b] Physics Department, Faculty of Science, Benha University, Benha, 13518, Egypt
[c] Laboratory of Nano-Smart Materials for Science and Technology (LNSMST), Department of Physics, Faculty of Science, King Khalid University, P.O. Box 9004, Abha, Saudi Arabia
[d] School of Chemistry and Chemical Engineering, Shanghai Electrochemical Energy Devices Research Center, Shanghai Jiao Tong University, Shanghai, 200240, China
[e] Department of Physics, Faculty of Science, Suez University, Suez, 43518, Egypt

ARTICLE INFO

Keywords:
Magnesium battery
Sulfur cathode
Halogen free electrolyte
Polysulfid imbolizer additives

ABSTRACT

Rechargeable magnesium–sulfur (Mg–S) and sodium–sulfur (Na–S) batteries are widely regarded as promising next-generation energy-storage systems due to their high theoretical energy density, intrinsic safety, and low material cost. However, their development remains fundamentally challenged by sluggish multivalent ion transport, unstable electrolyte–electrode interfaces, and severe polysulfide shuttling. In this work, we propose and explore the use of phosphoric acid (H_3PO_4) as an unconventional electrolyte modifier to regulate Mg^{2+} solvation behavior, ionic conductivity, and solid–electrolyte interphase (SEI) evolution in Mg–S cells, rather than as a finalized optimization strategy. In parallel, a multifunctional sulfur cathode composed of graphene nanoplatelets, silicon carbide, and barium titanate is designed as a model platform to examine combined electronic conductivity, polysulfide confinement, and mechanical stabilization effects. Electrochemical and structural analyses (EIS, CV, SEM, and EDS) are employed to assess how H_3PO_4-induced solvation and interfacial changes influence Mg^{2+} diffusion and charge-transfer processes, revealing both performance gains and inherent limitations. For comparison, the same sulfur composite is evaluated in Na–S cells using a $NaPF_6$-based electrolyte, where fast initial Na^+ transport is observed but rapid capacity fading persists due to unresolved polysulfide shuttling. Rather than demonstrating performance optimization, this study highlights the opportunities and constraints of solvation-chemistry engineering combined with advanced sulfur-cathode design, offering critical insights to guide future development of halogen-free, safe sulfur-based battery systems.

1. Introduction

The increasing demand for safe, sustainable, and high-energy rechargeable batteries has intensified global interest in multivalent-ion systems, particularly magnesium-ion batteries (MIBs). Magnesium offers several intrinsic advantages over lithium and sodium, including high volumetric capacity, dendrite-free deposition under suitable electrolytes, and natural abundance. When paired with sulfur cathodes, magnesium-sulfur (Mg-S) batteries combine high theoretical capacity with low material cost and environmental compatibility. Despite this promise, practical Mg-S systems suffer from slow Mg^{2+} transport, strong ion-ion coordination, polysulfide shuttling, and rapid passivation of the Mg anode. These limitations originate primarily from electrolyte solvation chemistry and interfacial reactions, highlighting the need for carefully engineered halogen-free electrolytes and cathode architectures [1–3]. [4,5,6] [7,8] Conventional chloride-based magnesium electrolytes, including $MgCl_2$ and organomagnesium chlorides such as HMDSMgCl, can support reversible Mg plating/stripping but suffer from severe intrinsic limitations [4]. These systems are highly corrosive, exhibit narrow anodic stability windows (<2.5 V vs. Mg/Mg^{2+}), and show poor compatibility with high-voltage and sulfur-based cathodes due to parasitic side reactions and polysulfide shuttling [9,10]. As a result, extensive efforts have shifted toward halogen-free electrolytes based on weakly coordinating anions such as $TFSI^-$, NO_3^-,

* Corresponding author.
** Corresponding author.
E-mail addresses: mmdesoky@suezuniv.edu.eg (M.M. El-Desoky), ISLAM.SHIHAH@fsc.bu.edu.eg (E. Sheha).

https://doi.org/10.1016/j.macse.2026.100060
Received 14 December 2025; Received in revised form 2 February 2026; Accepted 24 February 2026

fluorinated alkoxyborates (e.g., $B(hfip)_4^-$), and carboranes [11–13]. While these systems offer improved oxidative stability and reduced corrosivity, challenges remain; for example, $Mg(TFSI)_2$ electrolytes often require solvation control to mitigate passivation, whereas $Mg[B(hfip)_4]_2$ provides excellent stability at the expense of high cost and complexity. In our previous work [12], a simple halogen-free electrolyte based on magnesium nitrate ($Mg(NO_3)_2$) dissolved in a mixed solvent of acetonitrile and tetraethylene glycol dimethyl ether (ACN/G4) was developed for magnesium-sulfur (Mg-S) battery applications. The electrolyte demonstrated reversible Mg plating/stripping behavior, acceptable anodic stability, and reasonable ionic conductivity, enabling the construction of full Mg-S cells. In parallel, a multifunctional sulfur cathode incorporating polar additives such as silicon carbide (SiC) and barium titanate ($BaTiO_3$) was designed to anchor polysulfides, mitigate the shuttle effect, and enhance redox kinetics. In addition, a polymer-layer interface based on PVDF was introduced to isolate the Mg metal anode from the liquid electrolyte, leading to improved interfacial compatibility and reduced parasitic reactions. Despite these encouraging outcomes, several critical limitations were identified that constrained the practical performance of the system. The Mg-S cells suffered from rapid capacity fading and limited cycling stability, indicating insufficient long-term interfacial robustness. Moreover, sluggish Mg^{2+} transport and slow sulfur conversion kinetics persisted, originating from the strong solvation and coordination of Mg^{2+} ions in nitrate-based electrolytes. The formation of unstable interphase layers on the Mg anode, particularly under elevated temperatures, resulted in increased interfacial resistance and reduced Coulombic efficiency. Furthermore, although polar additives improved polysulfide anchoring, complete suppression of polysulfide dissolution was not achieved, leading to continuous loss of active material. These shortcomings clearly highlight that electrolyte solvation chemistry and interfacial stability remain the key bottlenecks in Mg-S batteries, thereby motivating the present work, which focuses on rational solvation-structure engineering and interfacial regulation to overcome these intrinsic limitations and achieve more stable and efficient Mg-S battery systems. Recent advances in electrolyte engineering for rechargeable magnesium batteries have demonstrated that weakening Mg^{2+}–anion contact ion pairing through phosphate-based solvent design can substantially enhance Mg plating/stripping reversibility and high-voltage stability [14]. In particular, co-ether phosphate electrolytes employing organic methyl phosphates were shown to suppress excessive TFSI decomposition, reduce interfacial resistance, and enable long-term dendrite-free Mg cycling at practical current densities. Despite these achievements, several intrinsic limitations remain unresolved. The reliance on bulky organic phosphate additives introduces synthetic complexity, limited tunability of interfacial chemistry, and incomplete elimination of residual contact ion pairs, which still contribute to gradual anion decomposition and moderate Coulombic inefficiencies. Moreover, the interfacial passivation chemistry in such systems is largely governed by steric effects rather than by direct chemical buffering or acid–base regulation at the Mg surface. These shortcomings motivate the exploration of a more chemically active and fundamentally simpler phosphate source. Inspired by this framework, the present work replaces organic methyl phosphates with inorganic phosphoric acid (H_3PO_4) as a multifunctional electrolyte component. Unlike neutral organic phosphates, H_3PO_4 offers dynamic proton-mediated coordination, in situ interfacial buffering, and the ability to chemically regulate Mg^{2+} solvation and surface reactivity [15]. This strategy enables a new electrolyte design paradigm that simultaneously addresses ion-pair dissociation, interfacial stability, and parasitic reaction suppression, thereby extending the phosphate concept beyond steric disruption toward chemically adaptive electrolyte engineering. In this work, a sulfur composite is proposed that combines graphene nanoplatelets and super carbon to establish a conductive framework, while silicon carbide (SiC) and barium titanate (BTO) are introduced as polar dielectric additives to potentially anchor polysulfides, limit their migration, and regulate the local electric field within the cathode [12,16]. Such a design is expected to suppress polysulfide shuttling, improve interfacial charge transfer, and enhance sulfur utilization, particularly during the initial discharge, with BTO further anticipated to facilitate Mg^{2+} access to active sulfur sites. To gain broader insight into electrode–electrolyte interactions in multivalent versus monovalent systems, analogous sodium–sulfur (Na–S) cells employing a $NaPF_6$-based electrolyte are also investigated as a comparative platform. Overall, this study aims to explore whether phosphate-driven solvation tuning, combined with dielectric-engineered sulfur cathodes, can mitigate key bottlenecks in Mg–S batteries by promoting favorable Mg^{2+} desolvation, stabilizing interfacial chemistry, and reducing polysulfide shuttling, thereby advancing halogen-free multivalent energy-storage concepts.

2. Experimental techniques

2.1. Preparation of halogen-free electrolyte (HFE)

A halogen-free electrolyte (HFE) was prepared using magnesium nitrate as the Mg^{2+} source. $Mg(NO_3)_2{\cdot}6H_2O$ (20 g, ≥99%, Sigma-Aldrich) was first dehydrated under vacuum at 100 °C for four days, yielding 15.29 g of anhydrous $Mg(NO_3)_2$. The dried salt was transferred into an argon-filled glovebox (O_2 and H_2O < 1 ppm) and dissolved in a mixed solvent consisting of 57.99 mL acetonitrile (ACN, anhydrous, ≥99.8%) and 27.47 mL tetraethylene glycol dimethyl ether (TEGDME, ≥99%). The solution was magnetically stirred at 500 rpm for 6 h at room temperature to ensure complete dissolution, forming the base halogen-free electrolyte (HFE). To investigate the influence of solvation and interfacial modification, phosphoric acid was introduced as an electrolyte additive. Specifically, 0.15 mL of H_3PO_4 (85 wt% in H_2O) was added to 15 mL of the base HFE, followed by stirring at 500 rpm for an additional 6 h to obtain the HFE–H_3PO_4 electrolyte. All electrolytes were stored in sealed containers inside the glovebox to prevent moisture uptake. The sulfur cathode for Mg–S cells was prepared through a composite design intended to examine combined electronic conductivity, polysulfide anchoring, and structural stability. Elemental sulfur (6 g, ≥99.5%) was mixed with graphene nanoplatelets (0.6 g, surface area ~500 $m^2\ g^{-1}$), silicon carbide (1.2 g, particle size <100 nm), barium titanate (0.6 g, ≥99%), and Supercarbon conductive carbon black (0.6 g) in 600 mL of deionized water. The suspension was homogenized by probe ultrasonication (500 W, 20 kHz) using a pulsed mode (10 s on/10 s off) for 30 min, followed by magnetic stirring at 700 rpm for 2 h at room temperature. The resulting mixture was dried under vacuum at 80 °C for 24 h to remove residual water. The dried composite was ground manually in an agate mortar for 3 h to obtain a fine and uniform powder. To promote interparticle contact, the powder was placed in a crucible, purged with argon, and subjected to microwave irradiation at 800 W for 10 s. After cooling to room temperature, poly (vinylidene fluoride) (PVDF, Mw ≈ 534,000) was added at a loading of 10 wt% as a binder, and the mixture was further ground for 30 min. The composite powder was then dispersed in N-methyl-2-pyrrolidone (NMP, anhydrous, ≥99.5%) to form a viscous slurry, which was stirred at 700 rpm for 4 h. The slurry was cast onto aluminum foil (20 μm thickness) using a doctor blade, dried under vacuum at 80 °C for 2 h, and punched into 12 mm diameter electrodes. The electrodes were stored in an argon-filled glovebox prior to cell assembly. For Na–S cells, the cathode composition was adjusted to emphasize sulfur utilization while maintaining electronic conductivity. The sulfur content was reduced to 25 wt%, with Supercarbon accounting for 75 wt% of the conductive matrix. This was achieved by adding 0.35 g of additional Supercarbon and 0.15 g of PVDF binder to 0.5 g of the previously prepared sulfur composite powder, followed by slurry preparation and electrode fabrication using the same procedure described above. Material characterization was conducted to evaluate the physicochemical properties of

both electrolytes and cathodes. Fourier-transform infrared (FTIR) spectroscopy (Bruker Alpha II) was employed to examine the chemical interactions associated with H_3PO_4 addition in the electrolyte. The morphology and elemental distribution of the cathodes were analyzed using scanning electron microscopy coupled with energy-dispersive X-ray spectroscopy (SEM/EDS, JEOL JCM-7000). Phase composition and crystallinity were assessed by X-ray diffraction (XRD, Rigaku Miniflex 600), while thermal stability was examined using thermogravimetric analysis (NEXTA STA). Electrochemical measurements were carried out using CR2032 coin cells assembled in an argon-filled glovebox. For Mg–S cells, magnesium metal was used as the anode with either HFE or HFE–H_3PO_4 as the electrolyte. For Na–S cells, sodium metal was employed as the anode with a conventional 1 M $NaPF_6$ electrolyte in ethylene carbonate/dimethyl carbonate (EC/DMC, 1:1 v/v). Electrochemical impedance spectroscopy (EIS, frequency range 100 kHz–10 Hz) and cyclic voltammetry (CV, scan rate 0.1 mV s^{-1}) were performed using a CHI604E electrochemical workstation to probe ion transport, charge-transfer behavior, and redox processes. Magnesium stripping/plating behavior was evaluated using symmetric cells to assess polarization characteristics. Long-term galvanostatic cycling of both Mg–S and Na–S cells was conducted using a Neware battery testing system (5 V, 10 mA).

3. Results and discussion

Fig. 1a shows the X-ray diffraction (XRD) pattern of the synthesized pristine sulfur cathode, which was engineered through a multicomponent formulation including sulfur (S), graphene nanoplatelets (GNP), silicon carbide (SiC), barium titanate (BTO), and super carbon (SC). The diffraction peaks marked in red correspond to orthorhombic sulfur, with a dominant peak at $2\theta \approx 23.1^{\circ}$, indexed to the (222) plane, confirming the presence of crystalline sulfur in the composite [17]. The peaks labeled in blue represent the perovskite phase of barium titanate (BTO), identified by reflections at (100), (110), and (111), suggesting the structural stability of BTO after the mild microwave treatment [18]. The presence of carbonaceous phases, including graphene nanoplatelets and super carbon, is evident from the broad peaks around $2\theta \approx 26.5^{\circ}$, assigned to the (002) planes of graphitic carbon (marked in magenta) [19]. Moreover, the distinct green peaks at $2\theta \approx 35.6^{\circ}$ and 71.8°, corresponding to the (220) and (311) planes of SiC, confirm the successful incorporation of silicon carbide nanoparticles into the cathode architecture. These components play complementary roles in improving electrical conductivity, structural integrity, and the mechanical robustness of the cathode matrix. The preservation of each phase indicates that the composite preparation protocol-comprising ultrasonic dispersion, low-temperature vacuum drying, and brief microwave exposure-was sufficient to ensure homogenous mixing and bonding without compromising crystallinity. Fig. 1b presents the differential scanning calorimetry (DSC) and thermogravimetric (TGA) analysis of the synthesized sulfur cathode composite, which comprises sulfur, graphene nanoplatelets (GNP), barium titanate (BTO), silicon carbide (SiC), and super carbon (SC). The DSC curve (black line) reveals the thermal events associated with the melting, decomposition, and structural transformations of the composite. In contrast, the red curve de-

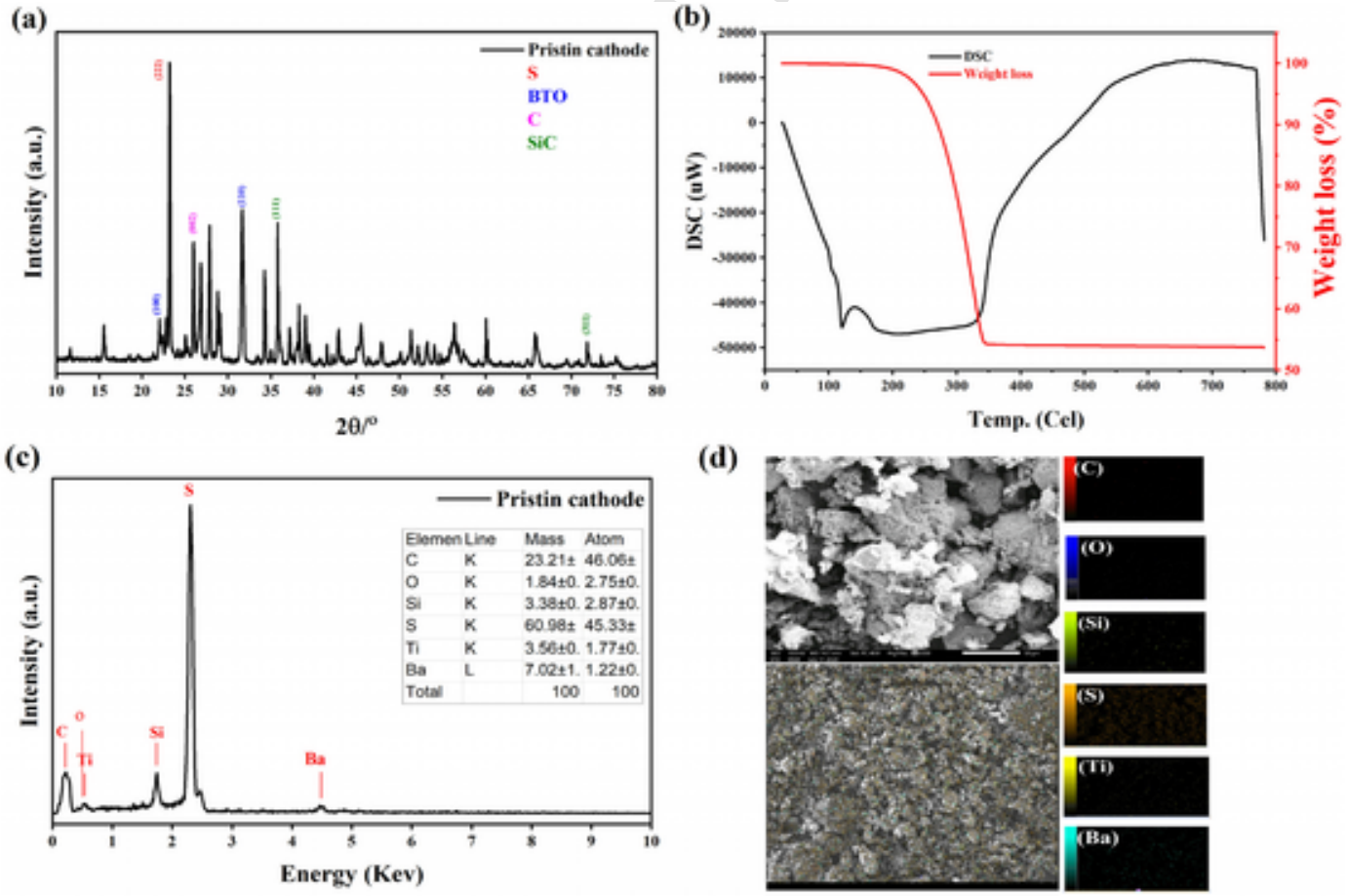

Fig. 1. Cathode Characterization: (a) X-ray diffraction (XRD) pattern, (b) differential scanning calorimetry (DSC) and thermogravimetric analysis (TGA) plots, (c) energy-dispersive X-ray spectroscopy (EDS) spectrum, and (d) scanning electron microscopy (SEM) images of the as-prepared cathode.

notes the corresponding weight loss percentage as the temperature increases. A prominent endothermic peak is observed around 120-125 °C, which corresponds to the melting of elemental sulfur [16]. This is followed by a sharp endothermic drop near 315-320 °C, which is aligned with the rapid decomposition and volatilization of sulfur, as evidenced by the simultaneous significant weight loss of approximately 45%, attributed primarily to the sublimation of sulfur species. Beyond 320 °C, the weight stabilizes at around 55%, indicating that the remaining thermally stable components, such as SiC, BTO, and carbonaceous additives, are present. The absence of additional steep mass loss confirms the high thermal stability of the composite matrix post-sulfur volatilization. These results verify that the engineered cathode structure maintains its thermal integrity under operational conditions and that sulfur is efficiently incorporated and subsequently released in a defined thermal window. Although $BaTiO_3$ is known to exhibit a tetragonal-to-cubic ferroelectric phase transition near ~120-130 °C, this transition is not resolved in the composite DSC signal. This is expected for two reasons: (i) the BTO content in the cathode is relatively low compared to sulfur, and (ii) the enthalpy of the BTO ferroelectric transition is much smaller than the latent heat associated with sulfur melting. As a result, the sulfur endotherm completely masks any subtle thermal anomaly that might arise from $BaTiO_3$ [20]. Fig. 1c illustrates the energy-dispersive X-ray spectroscopy (EDS) spectrum of the synthesized pristine sulfur cathode, revealing the elemental distribution within the composite structure. The EDS spectrum confirms the presence of key elements derived from the cathode's constituent materials: sulfur (S), carbon (C), silicon (Si), titanium (Ti), barium (Ba), and oxygen (O). A strong and dominant peak at approximately 2.3 keV corresponds to sulfur (S), which is the main electroactive component, comprising 60.98 ± 1.6 wt % and 45.33 ± 1.2 at. %, indicating the cathode's high sulfur loading necessary for enhanced Mg-ion storage capacity. The carbon signal (C K-line) is also significant, with 23.21 ± 1.4 wt% and 46.06 ± 2.8 wt%, originating from both graphene nanoplatelets and super carbon. Additional signals for silicon (Si), titanium (Ti), and barium (Ba) are detected, validating the successful incorporation of silicon carbide (SiC) and barium titanate (BTO) as functional additives. These elements are detected in minor yet meaningful proportions (e.g., Ba at 7.02 ± 1.6 wt %, Ti at 3.56 ± 0.86 wt%), suggesting their preserved presence post-synthesis and potential contributions to mechanical support, dielectric behavior, and electrochemical activity. Fig. 1d displays the SEM images and corresponding elemental mapping of the engineered sulfur cathode composite. The SEM micrograph (top-left) reveals a highly porous, irregularly aggregated morphology with micro-sized clusters formed from the combined constituents-sulfur, carbonaceous additives, and ceramic fillers. This porous architecture is beneficial for facilitating electrolyte infiltration and accommodating volume changes during cycling in Mg-S batteries. The accompanying elemental mapping images provide a detailed spatial distribution of the major elements within the composite. The sulfur (S) signal, represented in orange, is uniformly dispersed throughout the sample, confirming the homogeneous integration of active material. The carbon (C) signal (red) appears sparsely but distinctly localized, attributed to super carbon and graphene nanoplatelets, which are critical for ensuring a conductive network. Silicon (Si), barium (Ba), and titanium (Ti) are clearly identified via their respective mapping channels (green, cyan, and yellow), indicating successful and well-distributed inclusion of SiC and BTO nanoparticles. Fig. 2(a–d) show the FTIR spectra of the pure solvents, halogen-free electrolyte (HFE) before and after the addition of H_3PO_4. In the blanck HFE spectrum (black line), broad absorption bands at ~3430 cm^{-1} and ~2960 cm^{-1} correspond to O-H and C-H stretching vibrations, respectively. After the addition of H_3PO_4 (red line), the intensity of the O-H band increases. Notably, new peaks appear after introduction of H_3PO_4 at ~1140 cm^{-1} and ~1040 cm^{-1}, which are attributed to P = O and P-O stretching vibrations, confirming the successful incorporation of phosphate groups. Furthermore, the diminished intensity of the C = O (~1730 cm^{-1}) and C-O (~1250 cm^{-1}) bands suggests an interaction between phosphate species and the solvent matrix [21]. The low-frequency region (400-1000 cm^{-1}) also shows additional vibrations likely due to P-O-C and P-OH interactions, which are absent in the unmodified HFE [22]. These results indicate that H_3PO_4 introduces new functional groups and alters the coordination environment around Mg^{2+}. By comparing the pure solvents, the base HFE, and the HFE–H_3PO_4 electrolyte, the observed emergence of P = O and P–O bands and the modulation of solvent-related vibrations can be confidently attributed to coordination environment regulation rather than intrinsic solvent contributions. Scheme 1 depicting the proposed coordination structures of the halogen-free electrolyte (HFE) before and after phosphoric acid modification, visually represents a key chemical transformation in the electrolyte design. Initially, magnesium nitrate ($Mg(NO_3)_2$) is solvated by tetraethylene glycol dimethyl ether (TEGDME) and acetonitrile (CH_3CN), forming a solvated Mg^{2+} ion complex stabilized by the lone pairs on etheric oxygen and nitrile nitrogen atoms.

This configuration, while sufficient for basic Mg^{2+} solvation, presents high charge-transfer resistance and limited interfacial stability. Upon the addition of a small volume of phosphoric acid (H_3PO_4), as detailed in the experimental section, the coordination environment of Mg^{2+} shifts significantly. Phosphate species from H_3PO_4 begin to coordinate directly with Mg^{2+}, displacing some of the weaker coordinating ligands (especially nitrates and nitrile), forming a more robust Mg-O-P coordination network. However, the broad O–H vibrational band observed after H_3PO_4 modification of the HFE indicates excessive hydroxyl species, which can aggravate the passivation of the Mg anode. Fig. 3a displays Nyquist plots of the symmetric SS‖Electrolyte‖SS cells. The intercept on the real axis provides the bulk resistance R_b, which was used to calculate the bulk $\sigma_b = \frac{t}{R_b A}$.

Fig. 3b presents the Arrhenius plot of ionic conductivity (σ) as a function of inverse temperature (1000/T) for the SS‖HFE‖SS and SS‖HFE-H_3PO_4‖SS cells. The temperature dependence follows the Arrhenius equation [23]: $\sigma = \sigma_o \exp^{\frac{-E_a}{KT}}$, where σ is the conductivity, σ_o is the pre-exponential factor, E_a is the activation energy, and K is the Boltzmann constant (8.617×10^{-5} eV K^{-1}). Linear regression of ln(σ) vs. 1000/T yields activation energies of 0.0987 eV for SS‖HFE-H_3PO_4‖SS and 0.0956 eV for SS‖HFE‖SS.

Fig. 3c presents Cole-Cole plots ($-\varepsilon''$ vs. ε'), which characterize the dielectric behavior. The broader semicircle for the H_3PO_4 system indicates stronger dielectric relaxation and higher polarization losses, corresponding to the slower τ and enhanced matrix-ion interactions. Fig. 3d shows that the relaxation time (τ), calculated by $\tau = \frac{1}{2\pi f_{max}}$ [24], decreases with increasing temperature for both electrolytes. SS‖HFE-H_3PO_4‖SS shows slightly longer τ values, indicating complicated ionic relaxation dynamics. Fig. 4a displays the Nyquist plots of half-cells for HFE and HFE_H_3PO_4 before and after stripping. The plots clearly show a decrease in charge transfer resistance (R_{ct}), particularly in the presence of H_3PO_4. This indicates that the addition of H_3PO_4 alter the nature of the anode/electrolyte interface and facilitates Mg^{2+} ion transfer within the electrolyte. The stripping/plating results of Mg/HFE/Mg and Mg/HFE_H_3PO_4/Mg, as shown in Fig. 4b, reveal distinct differences in electrochemical performance over 100 h. The Mg/HFE/Mg system (black line) exhibits a relatively stable voltage profile with minor fluctuations, maintaining a consistent overpotential throughout the cycling period, indicating steady magnesium stripping and plating behavior. In contrast, It is noted that the Mg/HFE–H_3PO_4/Mg symmetric cell exhibits a higher overpotential during the initial ~40 h of plating/stripping. This behavior indicates an early-stage interfacial instability associated with the rapid formation and reorganization of a phosphate-rich interphase on the Mg surface. The linear sweep voltammetry (LSV) curves, Fig. 4c, for Mg/HFE/SS (black line) and Mg/HFE_H_3PO_4/SS (red line) show distinct electrochemical behaviors within the potential

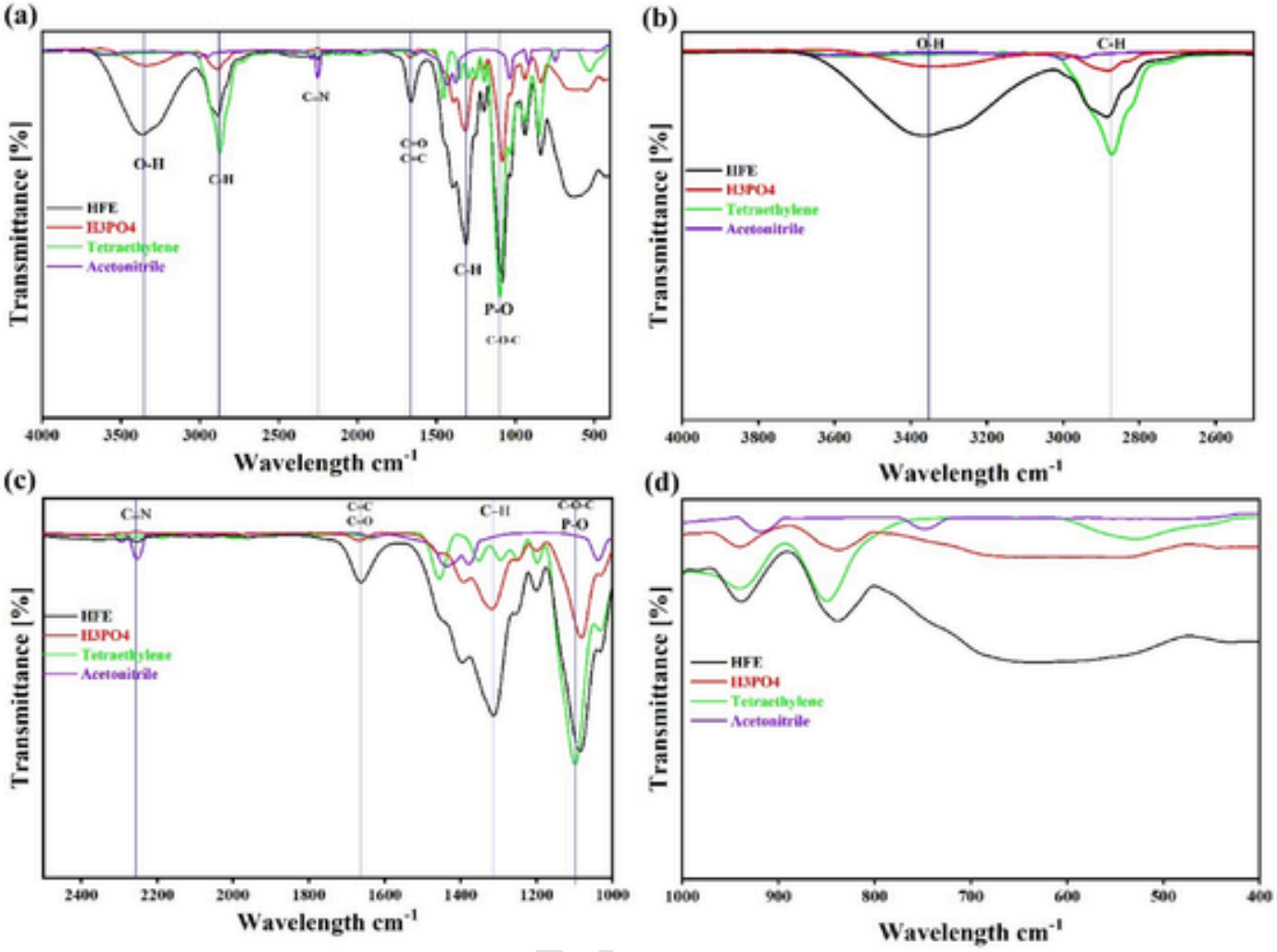

Fig. 2. (a) Full FTIR Spectra for the solvents and HFE and HFE_H_3PO_4 (b) 4000-2500. (c) 2500-1000. (d) 1000-400.

range of −1 to 5 V. The Mg/HFE/SS system exhibits a sharp increase in current density starting around 2 V, reaching approximately 5.76 mA at 5 V, indicating significant oxidative activity, likely due to electrolyte decomposition or magnesium dissolution. In contrast, the Mg/HFE_H_3PO_4/SS system displays a delayed onset of current increase, beginning near 3 V, and reaches a lower peak current of about 1.3 mA at 5 V, suggesting enhanced oxidative stability. The addition of H_3PO_4 to the HFE electrolyte likely forms a protective interfacial layer on the stainless steel (SS) electrode, suppressing unwanted side reactions and improving stability against oxidation. Thus, modifying the HFE electrolyte with H_3PO_4 plays a key role in enhancing electrochemical stability within this potential window. Fig. 4d presents the Nyquist plots of the half-cell before and after polarization, which were used to determine the bulk resistance (R_0) and interfacial resistance (R_s) for application of the Bruce–Vincent equation: $t_{Mg}{}^{+2} = \left[\frac{I_s(\Delta V - R_0 I_0)}{I_0(\Delta V - R_s I_s)}\right]$ [25]. The value of I_0 and I_s was extracted from Fig. 4e. The calculated results reveal significantly enhanced Mg^{2+} ion transport in the H_3PO_4-modified electrolyte. Specifically, the Mg^{2+} transference number reaches 0.627 for HFE–H_3PO_4, compared to 0.271 for pristine HFE, which is in good agreement with the electrochemical performance trends discussed above.

Fig. 5a presents the Nyquist plots derived from EIS measurements conducted on Mg/HFE/S and Mg/HFE_H_3PO_4/S cells before (B) and after (A) cyclic voltammetry (CV) treatment. The EIS spectra were fitted using an equivalent circuit, where the high-frequency semicircles correspond to the charge-transfer resistance (Rct) and the low-frequency tails reflect Warburg impedance associated with ion diffusion. Before CV, the Mg/HFE/S cell exhibits a large semicircle (~366 Ω) with a pronounced Warburg tail, indicating high interfacial resistance and sluggish ion transport. After CV, Rct increases markedly to ~630 Ω with an intensified Warburg response, suggesting interfacial degradation caused by Mg surface passivation and electrolyte decomposition. In contrast, the Mg/HFE–H_3PO_4/S cell shows a smaller Rct (~325 Ω) and a suppressed Warburg feature before CV, reflecting improved interfacial kinetics and ion diffusion. After CV, the resistance increases only slightly to ~408 Ω, while the Warburg contribution remains limited, demonstrating the stabilizing role of H_3PO_4 in maintaining a low-impedance interface. Overall, H_3PO_4 modification significantly reduces charge-transfer and diffusion resistances and effectively suppresses impedance growth upon cycling. Fig. 5b displays the low-frequency region of the EIS spectra plotted as Z′ versus $\omega^{-0.5}$ for Mg/HFE/S and Mg/HFE_H_3PO_4/S cells before and after cyclic voltammetry (CV), emphasizing the Warburg region associated with Mg^{2+} ion diffusion. The linear relationship in this low-frequency region According to equation $Z' = Rs + Rct + \sigma\,\omega^{-0.5}$ confirms diffusion-controlled behavior, and the slope (σ) of each line corresponds to the Warburg impedance, which can be used to estimate the Mg^{2+} dif-

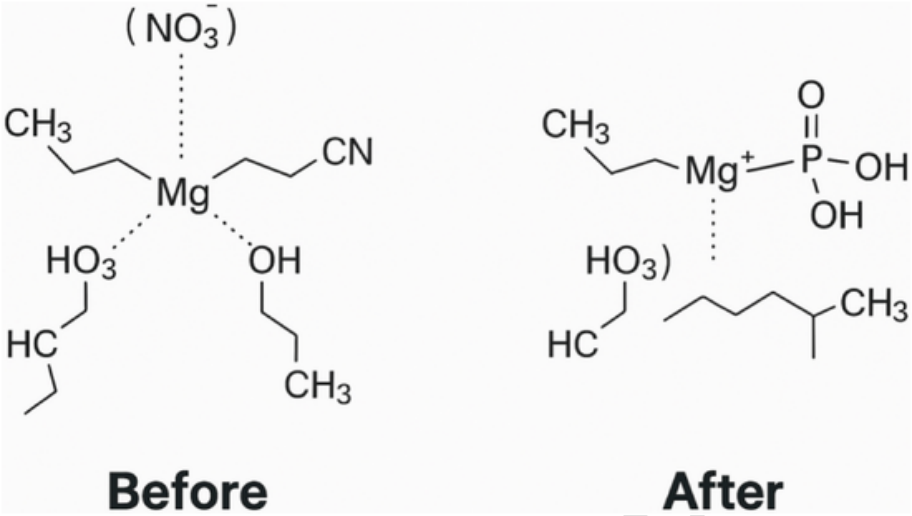

Scheme. 1. Coordination structure of $Mg(NO_3)_2$ with TEGDME and CH_3CN before (left) and after (right) modification by H_3PO_4, showing the replacement of nitrate coordination with phosphate ligands.

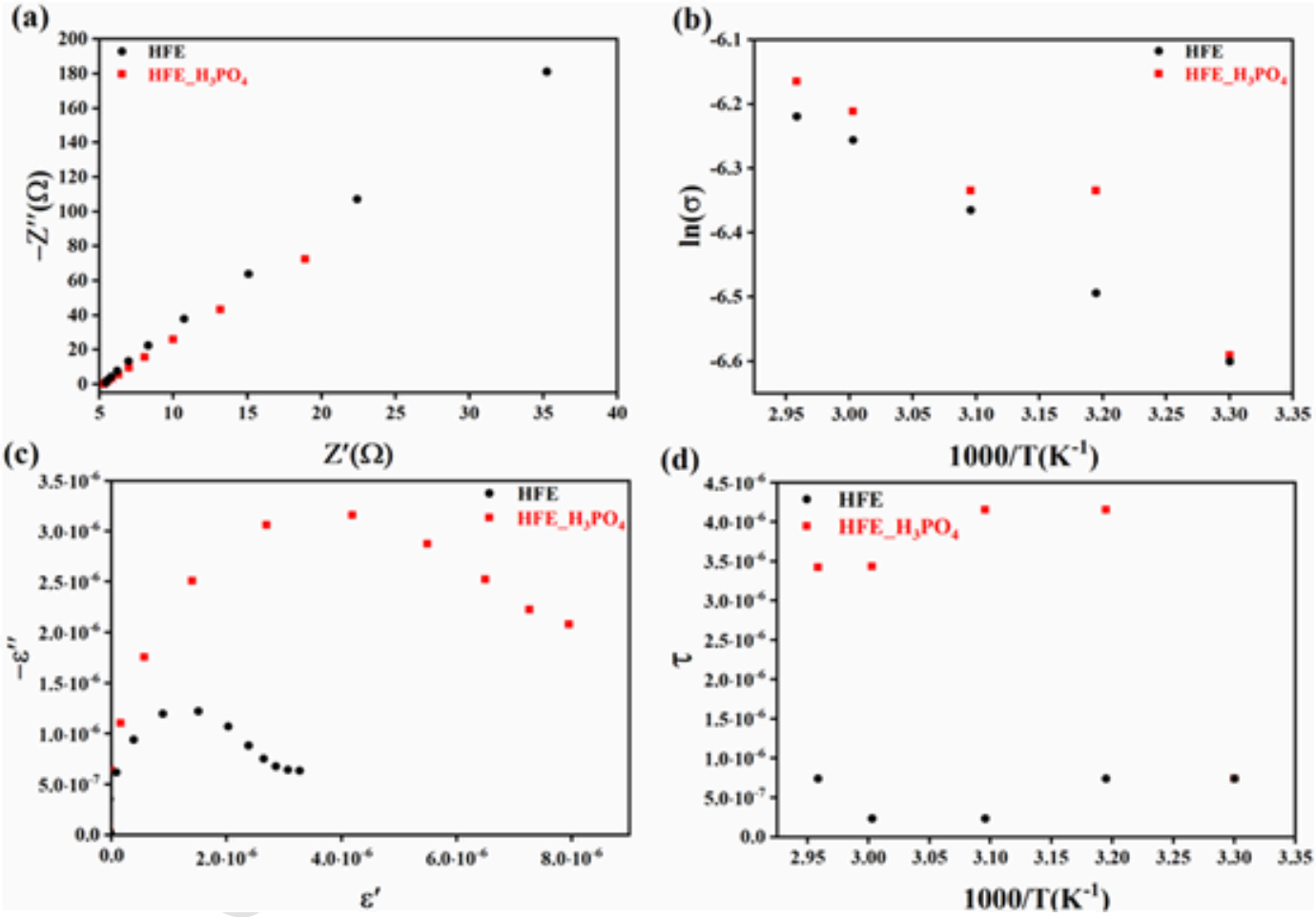

Fig. 3. (a) Nyquist plots. (b) Arrhenius plot. (c) Cole–Cole plot. (d)Relaxation time vs temperature; of HFE and H_3PO_4/HFE.

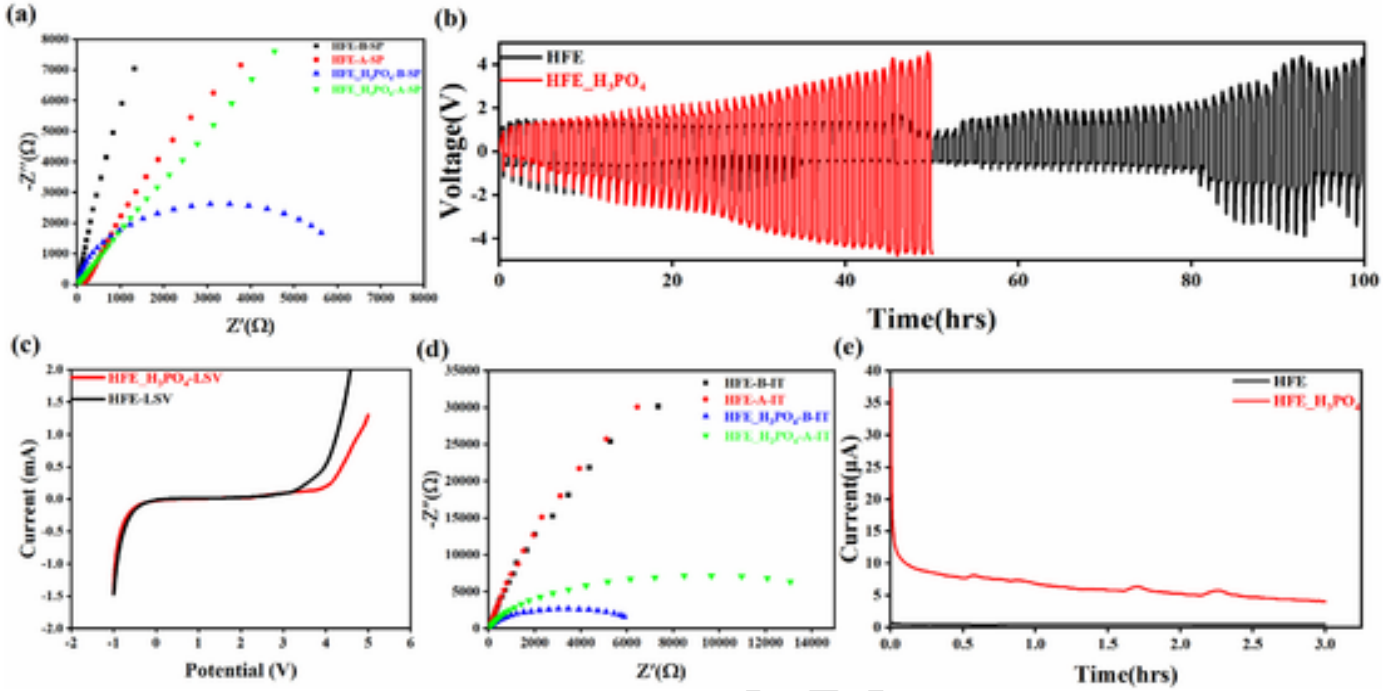

Fig. 4. (a) EIS spectra of symmetric cells before and after striping. (b) Stripping/plating of cells. (c) Linear sweep voltammetry (LSV). (d) Nyquist plot of cells before and after polarization. (e) Polarization current of cells; for HFE and HFE_H_3PO_4.

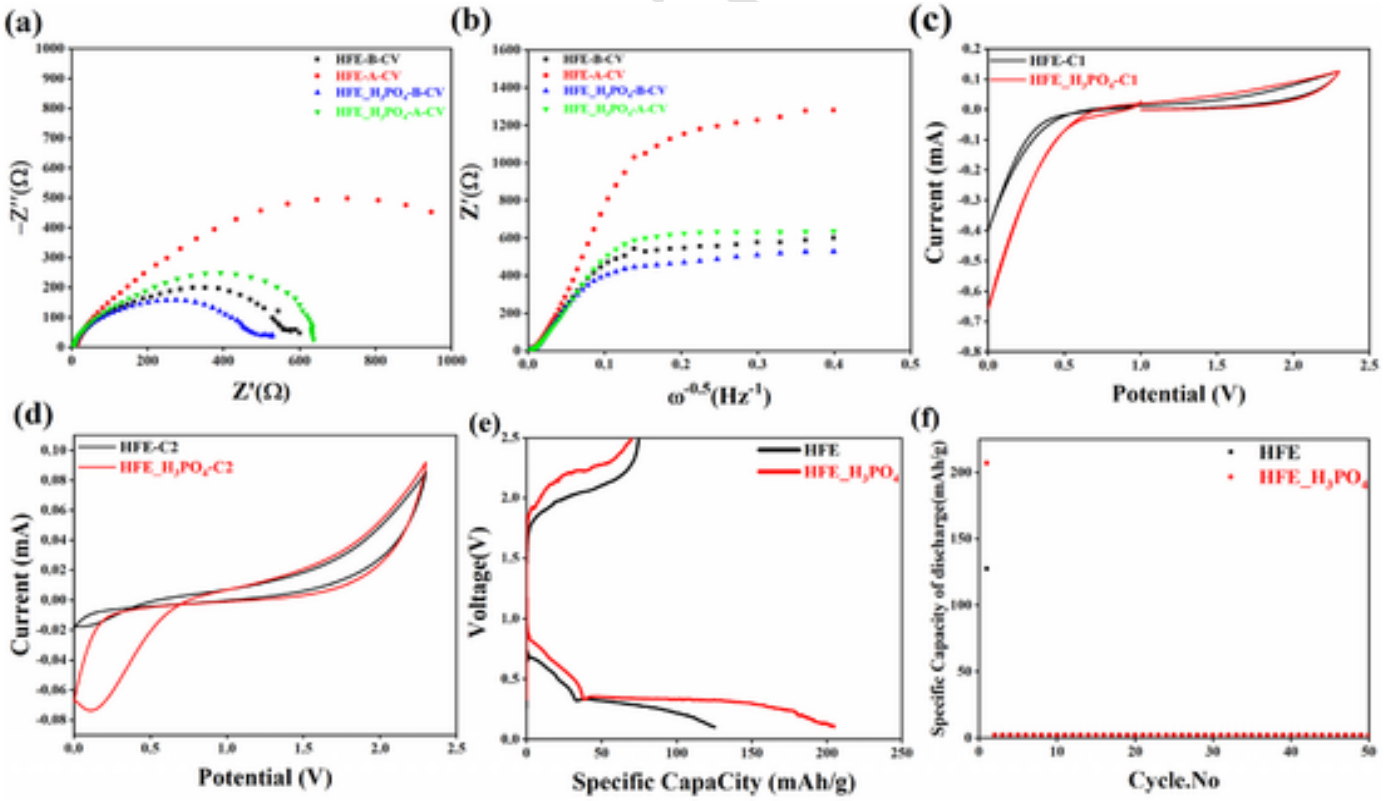

Fig. 5. (a) Nyquist plot with equivalent circuit. (b) ($\omega^{-0.5}$, Z′) linear fitting of Warburg impedance. (c) The first cycle of the CV curve. (d) The second cycle of the CV curve. (e) Discharge _ charge curves for H_3PO_4 and HFE cells. (f) Specific discharge capacity VS cycle No. of Mg | H_3PO_4/HFE | S Cells.

fusion coefficient using the equation $D_{Mg}{}^{+2} = [\frac{R^2T^2}{2A^2n^4F^4C^{22}}]$ [26]. Based on the estimated slopes, the calculated diffusion coefficients are 4.17×10^{-14} cm^2 s^{-1} for EIS_B_CV_HFE, 8.01×10^{-15} cm^2 s^{-1} for EIS_A_CV_HFE, 7.61×10^{-14} cm^2 s^{-1} for EIS_B_CV_H_3PO_4, and 8.97×10^{-13} cm^2 s^{-1} for EIS_A_CV_H_3PO_4 (green). The red curve exhibits the steepest slope and, hence, the lowest diffusion coefficient, indicating significant diffusion limitations after CV in the unmodified Mg/HFE/S cell. In contrast, the H_3PO_4-modified cells show consistently higher diffusion coefficients before and after CV, confirming the beneficial role of the additive in maintaining efficient Mg^{2+} transport. The cyclic voltammetry (CV) curves in Fig. 5c and d compare the electrochemical performance of Mg/HFE/S and Mg/HFE_H_3PO_4/S cells across two cycles. In representing cycle 1, the Mg/HFE/S cell exhibits a broad anodic peak at 1.8 V and a cathodic peak at 0.8 V, with a current density peaking at 0.2 mA/cm^2, indicating a reversible redox process with significant overpotential due to sluggish sulfur kinetics. The Mg/HFE_H_3PO_4/S cell in the same cycle shows a slightly shifted anodic peak at 1.7 V and a cathodic peak at 0.9 V, with a similar current density, suggesting that H_3PO_4 begins to influence the redox behavior even in the first cycle. It should be noted that the CV response of Mg–S cells is strongly influenced by rapid interfacial layer formation at both the Mg anode and the cathode–electrolyte interface. The fast growth of this interphase increases polarization and can partially suppress or broaden the redox peaks, particularly the anodic features, thereby obscuring a direct one-to-one correlation between peak positions and individual sulfur redox reactions. Consequently, the CV curves in Fig. 5c and d are discussed in terms of relative redox evolution and electrolyte-dependent behavior rather than definitive assignment of specific conversion steps. In Fig. 5d, representing cycle 2, the Mg/HFE/S cell maintains a similar profile to that of cycle 1, with an anodic peak at 1.8 V and a cathodic peak at 0.8 V; however, the current density decreases slightly, indicating possible degradation. Conversely, the Mg/HFE_H_3PO_4/S cell in cycle 2 displays two anodic peaks at 1.2 V and 2.0 V and two cathodic peaks at 0.8 V and 0.2 V, with a current density of 0.1 mA/cm^2, reflecting a multi-step redox process and improved sulfur utilization due to H_3PO_4. Fig. 5e and f compare the electrochemical performance of Mg/HFE/S and Mg/HFE_H_3PO_4/S cells in terms of their voltage profiles and cycling behavior. From the initial discharge curves in Fig. 5e, the Mg/HFE_H_3PO_4/S cell exhibits a significantly higher initial discharge capacity of approximately 210 mAh/g, compared to only 135 mAh/g for the Mg/HFE/S cell. This improvement suggests that incorporating H_3PO_4 into the electrolyte enhances sulfur redox kinetics and Mg^{2+} ion accessibility at the cathode-electrolyte interface. Furthermore, Fig. 5f illustrates the cycling performance over 50 cycles, where both cells demonstrate a sharp drop in capacity after the first cycle, indicating poor long-term cycling stability. However, the H_3PO_4-modified cell achieves a higher initial capacity, reinforcing its beneficial role in improving the initial electrochemical utilization of sulfur. Despite the similar capacity fading trends in subsequent cycles, the superior initial capacity of the H_3PO_4-based system highlights the potential of electrolyte additives in optimizing Mg-S battery performance. Although the Mg–S cells were cycled for ~50 cycles, a pronounced capacity drop occurs after the first cycle, followed by rapid fading, indicating limited long-term cycling stability. Quantitatively, the capacity retention after 50 cycles is only a small fraction of the initial discharge capacity, underscoring the persistence of interfacial degradation and polysulfide loss. Therefore, the present results demonstrate only a relative improvement in early-stage electrochemical behavior rather than sustained long-term cycling stability. Extended cycling over ≥100 cycles will be required in future studies to fully validate electrolyte robustness and interfacial durability. The initial discharge capacity of the Mg–S cells (~205–210 mAh g^{-1}) is lower than that reported in several recent Mg–S studies. For example, Ref. [27] demonstrates that advanced electrolyte designs capable of weakening Mg^{2+} ion pairing can substantially enhance Mg transport and sulfur utilization, while Ref. [28] highlights that even when ion transport is improved, sulfur-based cells remain strongly limited by interfacial instability and polysulfide shuttling. In comparison, the present halogen-free nitrate electrolyte offers improved interfacial regulation relative to the baseline system but still suffers from strong Mg^{2+} solvation and incomplete polysulfide confinement, which togeowardther restrict the achievable capacity. To provide a broader and comparative understanding of how solvation chemistry and electrode architecture influence sulfur redox behavior, both Mg-S and Na-S systems are examined within the same study. The Mg-S cell serves as the primary platform for evaluating the impact of halogen-free electrolyte engineering and phosphate-modified solvation structures on multivalent ion transport. In parallel, the Na-S cell-employing the same sulfur composite cathode but a conventional $NaPF_6$ electrolyte-acts as a monovalent reference system. Fig. 6a presents the Nyquist plots of the Na-S battery system before (EIS_B_CV) and after (EIS_A_CV) cyclic voltammetry testing. Both spectra exhibit typically depressed semicircles at high-to-medium frequencies followed by a sloped line at low frequencies, indicating a combination of charge transfer resistance and ion diffusion processes. Notably, the impedance spectra recorded after CV (EIS_A_CV, red curve) shows a reduced overall semicircle diameter compared to the pre-CV data (EIS_B_CV, black curve), reflecting a decrease in charge transfer resistance (R_{ct}). This reduction suggests an enhancement in interfacial charge transport, likely attributed to improved electrode-electrolyte contact and activation of the composite cathode during cyclic voltammetry (CV) cycling. Moreover, the lower intercept on the Z′-axis in the post-CV spectrum implies a slight decrease in bulk resistance (R_s), which may result from improved electrolyte penetration or rearrangement within the cathode's porous structure. Overall, the EIS analysis confirms that electrochemical activation through CV enhances ionic/electronic conductivity and facilitates more efficient redox kinetics in the engineered Na-S system. Fig. 6b presents the low-frequency region of the EIS spectra plotted as Z′ versus $\omega^{-0.5}$ for Na/$NaPF_6$/S and Na/$NaPF_6$/S cells before and after cyclic voltammetry (CV). Based on the linear Warburg region of the EIS plot (Z′ vs $\omega^{-0.5}$), the sodium-ion diffusion behavior was analyzed using the equation: $Z' = Rs + Rct + \sigma\,\omega^{-0.5}$ where σ is the Warburg coefficient (slope of the linear region), and it is directly related to the ion diffusion process. The diffusion coefficient for Na^+ was calculated using the following expression: $D_{Na}{}^{+} = [\frac{R^2T^2}{2A^2n^4F^4C^{22}}]$ n = 1, Slopes (σ) from the plot: 350 Ω $s^{-0.5}$ (before CV), 300 Ω $s^{-0.5}$ (after CV). The calculated diffusion coefficients $D_{Na}{}^{+}$ are: ≈2.89×10^{-13} cm^2/s Before CV and ≈3.94×10^{-13} cm^2/s After CV. This enhancement in diffusion coefficient after CV confirms that electrochemical activation improves Na^+ mobility within the electrode matrix, further validating the diffusion-controlled behavior of the Na-S battery system. Fig. 6c illustrates the cyclic voltammetry (CV) profiles for the Na-S battery employing a multi-component sulfur cathode and a $NaPF_6$-based electrolyte. The electrolyte system consists of 1 M $NaPF_6$ in EC/DMC (1:1 v/v) with sodium metal serving as the counter/reference electrode. The CV curves across the first four cycles (Cyc1-Cyc4) demonstrate a pair of redox peaks associated with the reversible conversion of sulfur species, indicating stable electrochemical behavior. The initial cycle (Cyc1) shows slightly broader peaks and higher overpotential, which stabilizes in subsequent cycles, reflecting the electrochemical activation of the composite cathode. The minimal shift in peak positions and consistent current response in later cycles highlight promising cycling stability and electrochemical reversibility of the designed Na-S system. These results underscore the effectiveness of cathode engineering in enhancing sodium storage kinetics and suggest that the tailored composite facilitates efficient redox conversion, aligning with the broader goal of developing robust sulfur cathodes for both sodium and magnesium rechargeable batteries. The cycling behavior of the Na/$NaPF_6$/S cell was evaluated to understand the electrochemical reversibility and capacity retention of the designed sulfur cathode. As shown in Fig. 6d, the initial discharge-charge profile (Cycle

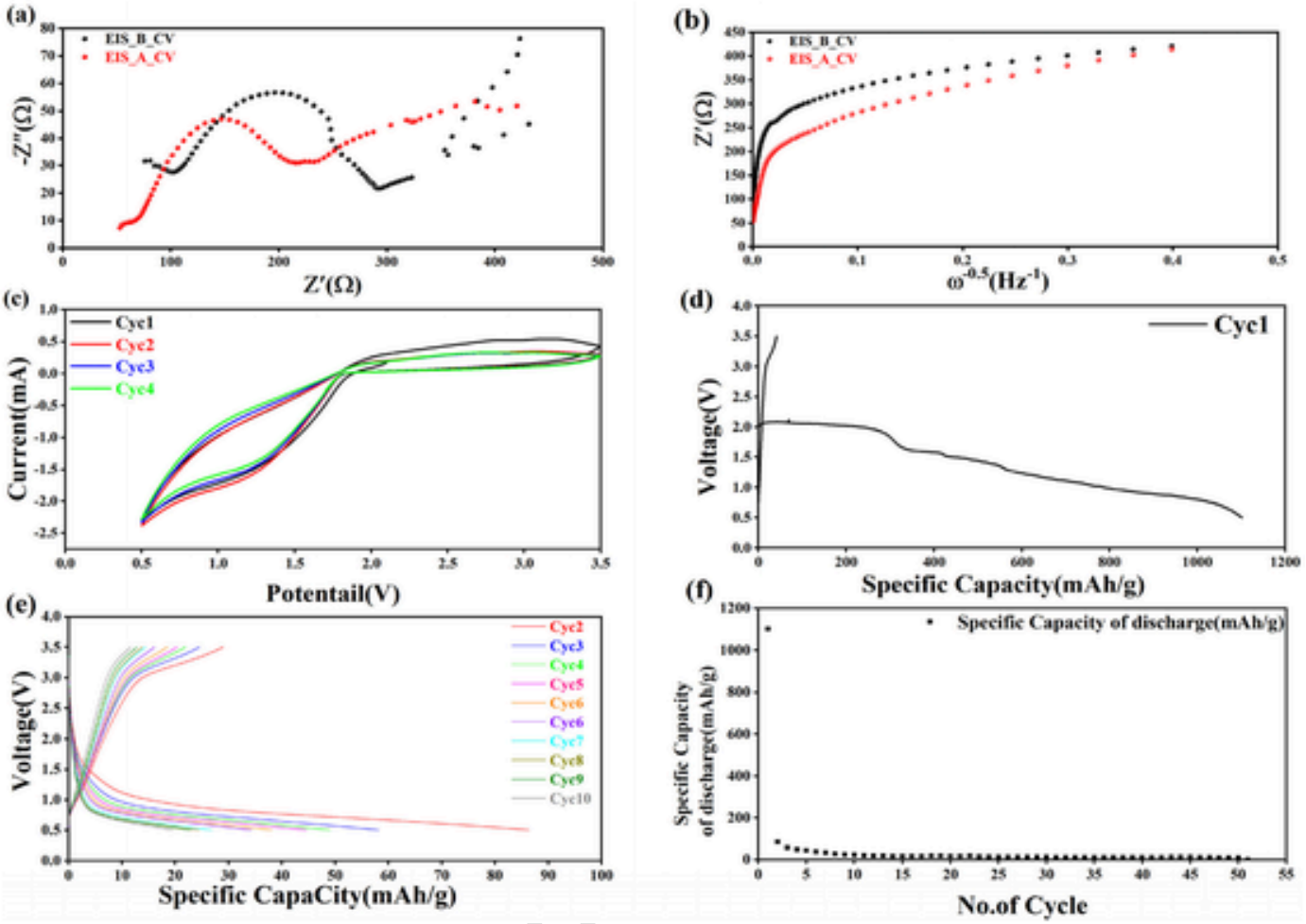

Fig. 6. (a) Nyquist plot with an equivalent circuit. (b) ($\omega^{-0.5}$, Z′) linear fitting of Warburg impedance. (c) Cycles of CV curve. (d) The initial discharge _ charge curve for (Na_S) cells. (e) Discharge _ charge curves for (Na_S) cells. (f) Specific discharge's capacity VS cycle No. of Na||$NaPF_6$||S Cells.

1) reveals a high specific capacity of approximately 1101 mAh/g, with a sloping voltage plateau beginning near 2.0 V and gradually declining to around 0.5 V. This broad discharge region corresponds to the multi-step conversion of elemental sulfur into various sodium polysulfides (Na_2S_n), indicative of a typical sodium-sulfur electrochemical process. However, subsequent cycles, as presented in Fig. 6e, demonstrate a significant reduction in specific capacity, dropping to below 30 mAh/g by Cycle 10. The disappearance of the clear plateau and the compression of capacity values in the following cycles suggest a high degree of polarization and limited reversibility, likely due to growth of undesired species at the surface of Na anode and polysulfide dissolution, as well as poor Na^+ diffusion or sluggish kinetics in the cathode composite. Despite this, the voltage profiles maintain a quasi-linear shape during discharge and charge, reflecting some degree of reversible redox activity. The long-term cycling performance of the Na/$NaPF_6$/S cell is presented in Fig. 6f, showing the evolution of discharge capacity over 52 cycles. The initial discharge capacity reaches approximately 1101 mAh/g, highlighting the high sodium storage capability of the sulfur-based cathode. However, a sharp and rapid capacity fade is observed after the first few cycles. By the fifth cycle, the capacity drops below 50 mAh/g and continues to decline gradually, stabilizing at around 10 mAh/g from cycle 25 onwards. This severe capacity decay is indicative of poor cycling stability, likely caused by irreversible side reactions, polysulfide dissolution, and shuttle effects, as well as the limited structural integrity of the composite cathode. The rapid capacity fading indicates that further optimization of cathode structure or electrolyte formulation may be necessary to enhance long-term cycling stability in Na-S systems. It should be emphasized that the Na–S cathode employed in this study contains a relatively low sulfur loading (25 wt% S), which was intentionally selected to ensure sufficient electronic conductivity and to probe electrolyte–sulfur redox behavior rather than to achieve practical energy density.

4. Conclusion

This study investigated phosphate-driven solvation regulation and multifunctional sulfur cathode design as a mechanistic approach to address key limitations in Mg–S and Na–S batteries. Introducing a small amount of H_3PO_4 into a halogen-free $Mg(NO_3)_2$ electrolyte alters the Mg^{2+} coordination environment, leading to higher Mg^{2+} transference number, reduced charge-transfer resistance, improved oxidative stability, and enhanced Mg^{2+} diffusion. These effects result in improved initial sulfur utilization and more stable interfacial impedance behavior. However, the presence of hydroxyl species associated with H_3PO_4 also promotes Mg surface passivation, causing elevated early overpotential and continued capacity fading during cycling. This highlights a trade-off between improved solvation kinetics and long-term interfacial stability. The engineered sulfur cathode enhances initial redox activity in both Mg–S and Na–S systems but cannot fully suppress polysulfide shut-

tling or long-term degradation. Overall, this work demonstrates that chemically active phosphate additives and dielectric-assisted cathode architectures can improve early electrochemical performance but remain insufficient for sustained cycling stability. The results provide important insights to guide future halogen-free electrolyte designs that balance solvation control with interfacial durability in sulfur-based battery systems.

CRediT authorship contribution statement

Manal Bin Zaima: Validation, Investigation. **Hassan Manaa:** Formal analysis, Data curation. **Osama Ragab:** Methodology, Investigation. **Ibrahim S. Yahia:** Software, Investigation. **Yanna NuLi:** Investigation, Formal analysis. **M.M. El-Desoky:** Writing – review & editing, Supervision. **Eslam Sheha:** Writing – original draft, Supervision.

Declaration of competing interest

The authors declare that they have no known competing financial interests or personal relationships that could have appeared to influence the work reported in this paper.

Acknowledgement

The authors extend their appreciation to the Deanship of Research and Graduate Studies at King Khalid University for funding this work through Large Research Project under grant number RGP2/648/46.

Data availability

Data will be made available on request.

References

[1] H. Zhang, L. Qiao, M. Armand, Organic electrolyte design for rechargeable batteries: from lithium to magnesium, Angew. Chem. Int. Ed. 61 (2022) e202214054.
[2] S.A. Mahmood, N.N. Mobarak, M.F. Shibl, K.A. Soliman, DFT insights into the role of penta-SiC_2 in enhancing Li–S battery performance through polysulfide anchoring, Mater. Chem. Phys. 332 (2025) 130236.
[3] C.B. Bucur, T. Gregory, A.G. Oliver, J. Muldoon, Confession of a magnesium battery, J. Phys. Chem. Lett. 6 (2015) 3578–3591.
[4] L. Sheng, J. Feng, M. Gong, L. Zhang, J. Harding, Z. Hao, F.R. Wang, Advances and challenges in electrolyte development for magnesium–sulfur batteries: a comprehensive review, Molecules 29 (2024) 1234.
[5] W. Teng, J. Wu, Q. Liang, J. Deng, Y. Xu, Q. Liu, B. Wang, T. Ma, D. Nan, J. Liu, Designing advanced liquid electrolytes for alkali metal batteries: principles, progress, and perspectives, Energy Environ. Mater. 6 (2023) e12355.
[6] Y. Man, P. Jaumaux, Y. Xu, Y. Fei, X. Mo, G. Wang, X. Zhou, Research development on electrolytes for magnesium-ion batteries, Sci, Bull. 68 (2023) 1819–1842.
[7] H. Fan, Y. Zhao, J. Xiao, J. Zhang, M. Wang, Y. Zhang, A Non-nucleophilic gel polymer magnesium electrolyte compatible with sulfur cathode, Nano Res. 13 (2020) 2749–2754.
[8] A. Schmidt, H. Koger, A. Barthélemy, G. Studer, B. Esser, I. Krossing, Is one of the least coordinating anions suitable to serve as electrolyte salt for magnesium-ion batteries? Batter. Supercaps 5 (2022) e202200340.
[9] Y. Shen, K. Xu, Z. Zhao-Karger, X. Zhao, Tailoring loose Mg2+ solvation structure by steric and competitive solvent coordination for fast-charging magnesium batteries, Energy Environ. Mater., e70124..
[10] Development of calcium electrolytes for post-lithium-ion batteries with enhanced charge transfer kinetics, in: 서울대학교 대학원, 2025.
[11] S. Fan, G.M. Asselin, B. Pan, H. Wang, Y. Ren, J.T. Vaughey, N. Sa, A simple halogen-free magnesium electrolyte for reversible magnesium deposition through cosolvent assistance, ACS Appl. Mater. Interfaces 12 (2020) 10252–10260.
[12] E. Sheha, M. Farrag, S. Fan, E. Kamar, N. Sa, A simple Cl—free electrolyte based on magnesium nitrate for magnesium–sulfur battery applications, ACS Appl. Energy Mater. 5 (2022) 2260–2269.
[13] Z. Zhao-Karger, R. Liu, W. Dai, Z. Li, T. Diemant, B.P. Vinayan, C. Bonatto Minella, X. Yu, A. Manthiram, R.J. Behm, M. Ruben, M. Fichtner, Toward highly reversible magnesium–sulfur batteries with efficient and practical Mg[B(hfip)4]2 electrolyte, ACS Energy Lett. 3 (2018) 2005–2013.
[14] C. Li, R.D. Guha, A. Shyamsunder, K.A. Persson, L.F. Nazar, A weakly ion pairing electrolyte designed for high voltage magnesium batteries, Energy Environ. Sci. 17 (2024) 190–201.
[15] L. Zhang, H. Lu, B. Cheng, Y. Ding, H. Yang, Effect of H3PO4 additive on wear resistance and acid protection of plasma electrolytic fluorination coating on magnesium alloy, Ceram. Int. 51 (2025) 21484–21500.
[16] L. Zhou, O. Ragab, N. Wally, K.F. Qasim, X. Li, M. El-Desoky, W. Xing, E. Sheha, The interplay between different potassium electrolytes and MoS 2@ SiC@ S cathodes in the performance of potassium–sulfur batteries, RSC Adv. 14 (2024) 37902–37910.
[17] J. Shao, Z. Wang, H. Wang, X. Ma, X. Wang, H. Wang, H. Huang, J. Ren, R. Wang, Polysulfide conversion enhanced by the synergistic effect of anthraquinone and Fe-N4 on sulfur crystals, J. Power Sources 639 (2025) 236650.
[18] L.K. Linke, K.E. Dehm, K. Gubanov, R.H. Fink, B.M. Szyja, R.W. Crisp, Colloidal organometallic synthesis of solution-processable barium titanate nanoparticles for nanoelectronic applications, Nanoscale 17 (2025) 7917–7925.
[19] H. Zhang, Z. Meng, X. Zhao, S. Wang, J. Huang, Y. Min, Highly graphitized carbon film derived from Al2O3@ Talc-polyimide composite and its application as high-performance anode material in lithium-ion battery, Diam. Relat. Mater. (2025) 112023.
[20] N. Yacout, H. Refai, M.A. Kebede, F. Salman, E. Sheha, Significant study of BaTiO3 as a cathode for magnesium battery applications, Mater. Chem. Phys. 292 (2022) 126770.
[21] B.H. Stuart, Infrared Spectroscopy: Fundamentals and Applications, John Wiley & Sons, 2004.
[22] K. Nakamoto, Infrared and Raman Spectra of Inorganic and Coordination Compounds, Part B: Applications in Coordination, Organometallic, and Bioinorganic Chemistry, John Wiley & Sons, 2009.
[23] M. Attallah, E. Sheha, Tailoring the electrochemical performance of the polymer electrolyte using Na2H20B4O17 for magnesium sulfur battery applications, Curr. Appl. Phys. 71 (2025) 175–183.
[24] Y. Abe, P.J. Flory, Configurational statistics of 1,4-Polyisoprene chains, Macromolecules 4 (1971) 230.
[25] M. Radi, T. Purkait, D.S. Tchitchekova, A.R. Goñi, R. Markowski, C. Bodin, C. Courrèges, R. Dedryvère, A. Ponrouch, A comprehensive study on the parameters affecting magnesium plating/stripping kinetics in rechargeable Mg batteries, Adv. Energy Mater. 14 (2024) 2401587.
[26] Y. Sun, H. Cui, X. Yan, X. Zhang, X. Zhao, Z. Kou, B. Liu, Z. Cheng, Copper-powder/Ni-MOF derivatives for superior conductivity in magnesium-sulfur battery cathodes, J. Alloys Compd. 1026 (2025) 180551.
[27] Z. Zhao-Karger, R. Liu, W. Dai, Z. Li, T. Diemant, B. Vinayan, C. Bonatto Minella, X. Yu, A. Manthiram, R.J.r. Behm, Toward highly reversible magnesium–sulfur batteries with efficient and practical Mg [B (hfip) 4] 2 electrolyte, ACS Energy Lett. 3 (2018) 2005–2013.
[28] M. Rashad, M. Asif, Z. Ali, Quest for magnesium-sulfur batteries: current challenges in electrolytes and cathode materials developments, Coord. Chem. Rev. 415 (2020) 213312.